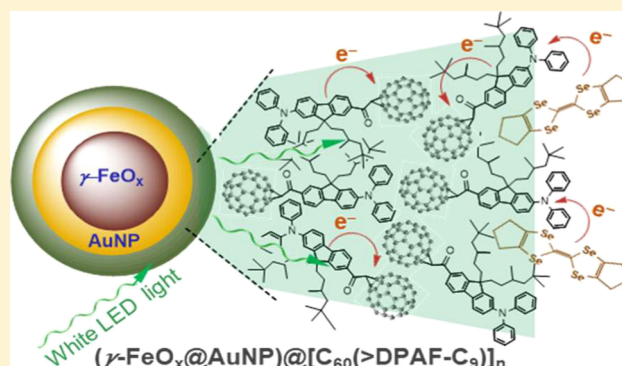# Enhancement of Photoswitchable Dielectric Property by Conducting Electron Donors on Plasmonic Core−Shell Gold-Fluorenyl C$_{60}$ Nanoparticles

Min Wang,[†] Tzuyang Yu,[‡] Loon-Seng Tan,[§] Augustine Urbas,[§] and Long Y. Chiang[*,†]

[†]Department of Chemistry and [‡]Department of Civil and Environmental Engineering, University of Massachusetts Lowell, Lowell, Massachusetts 01854, United States

[§]Functional Materials Division, AFRL/RXA, Air Force Research Laboratory, Wright-Patterson Air Force Base, Dayton, Ohio 45433, United States

S *Supporting Information*

ABSTRACT: A new nanomaterial design was made by the construction of a tetralayered core−shell configuration, containing a magnetic core of nanospherical γ-FeO$_x$ particle (NP) encapsulated by one plasmonic gold subshell, one middle layer of electron-polarizable C$_{60}$(>DPAF-C$_n$)$_x$-derived fullerosome membrane, and an outer shell of organic electron donors. This class of multilayered core−shell nanospherical materials was recently reported to be excellent microwave absorbers. We found that this analogous of multilayered NPs was capable of inducing photoswitchable dielectric property (permittivity) amplification at the microwave frequency range of 1.0−4.0 GHz. The enhanced phenomena were further investigated by the use of six variable organic molecular electron donors and two conducting conjugated polymers, serving as the supply of photoinduced transferrable electrons at the outer shell layer, for comparison. The design largely increased the number of polarizable charges, leading to a maximum of 387% amplification of the relative dielectric constant (ε_r') value or a 159% additional increase from that of the parent trilayered precursor NPs without organic donors. The latter percentage increase of ε_r' was contributed from the application of electron-donating hexamethylenetetraselenafulvalene molecules. Good recyclability of relative complex dielectric properties (ε_r' and the derivative ε_r'') back to their original values during each photoactivation cycle of light-on and light-off manipulations may allow the potential nanomaterial uses as photoswitchable dielectrics in the modulation of microwave reflection signals.

INTRODUCTION

Phenomena of photoswitchable amplification of dielectric properties at radio frequency (rf) and microwave frequency (0.5−18 GHz) were relatively new and reported only recently.[1,2] They were detected under a photoinduced electron-transfer mechanism upon in situ generation of the surface plasmon resonance (SPR) energy at the near-field interfacial layer of trilayered core−shell nanospherical particles (NPs). Examples were given by the use of electron-polarizable C$_{60}$-(diphenylamino-dialkylfluorene)$_x$, C$_{60}$(>DPAF-C$_n$)$_x$, diads ($x = 1$), triads ($x = 2$), and pentaads ($x = 4$) as donor−acceptor conjugates deposited at the outer shell layer.[3,4] Observed large increase of dielectric properties was characterized by the initiation of intramolecular electron transfer from the diphenylaminofluorene donor moiety to the electron-accepting C$_{60}$> cage moiety, resulting in the formation of charge-separated (CS) (C$_{60}$>)$^{-n\bullet}$-[(diphenylaminofluorene)$^{+\bullet}$]$_n$ transient states. Interestingly, the detected photoswitching effect was attributed to the occurrence of SPR energy accumulation

that fits well with the predicted light-trapping effect, leading to the concentration of or folding the incident photon energy into enhanced plasmon oscillations in a thin-film layer.[5] The effect was proposed to be achievable by embedding SPR-producing semiconducting NPs in the dielectric medium to potentially rise its dielectric property.[6,7] In our recent examples of trilayered core-shelled (γ-FeO$_x$@AuNP)@[C$_{60}$(>DPAF-C$_9$)$_x$]$_n$ NPs,[8] condensed energy confinement in plasmonic oscillations localized within the interfacial area of shell layers can be transferred to the subsequent surrounding layers to induce intramolecular charge separation among donor and acceptor moieties of C$_{60}$(>DPAF-C$_9$)$_x$ nanoconjugates. The effect serves as the base of the photoinduced dielectric amplification.

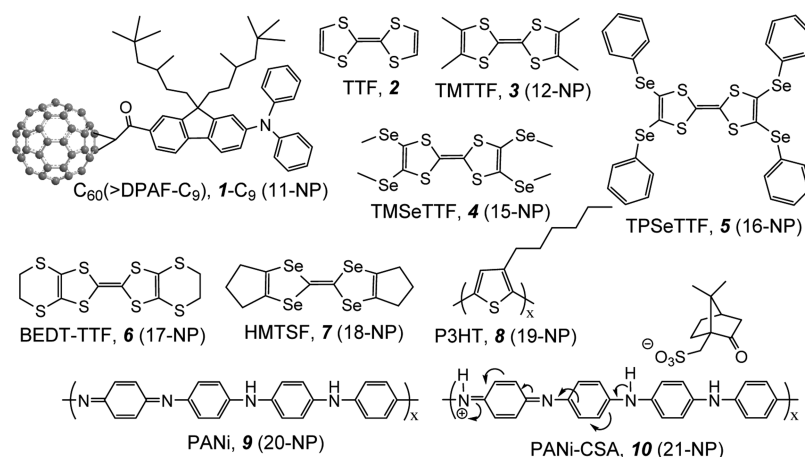Tetrathiafulvalene (TTF) and tetramethyltetrathiafulvalene (TMTTF) are traditional, classic electron-conducting organic

Figure 1. Compound structure of [60]fullerene−chromophore conjugates 1-C_9, several electron-donor molecules 2−7, and conducting polymers 8−10 with the corresponding core−shell nanoparticle assignment in parenthesis.

donors.[9,10] They possess reversible redox cycles with two low potentials of electron oxidation to their monocation radical and dication derivatives. Unusually, high stability of the cationic TTF radical was reasoned by the aromatic π-electron nature of the oxidized 1,3-dithiolium rings. Semiconducting properties of cationic TTF and the metallic behavior of TTF−tetracyanoquinodimethane (TCNQ)[11] and TMTTF−TCNQ[12] charge-transfer complexes have demonstrated efficient electron transport among molecular stacks of materials in a mixed valence state. By condensing the TTF ring with dithiophenyl moieties to the corresponding dithienotetrathiafulvalene[13,14] or dithiin moieties to result in bis(ethylenedithio)-tetrathiafulvalene (BEDT-TTF), intermolecular electronic π−π interactions among molecular stacking in a two-dimensional mixed valence structure can be extended beyond the core region of TTF. Especially, the latter was found to involve noncovalent interactions of −S···S− among stacking molecules[15] that was proposed to be the main contributing factor to the detected ambient pressure superconductivity.[16] When sulfur atoms were replaced by selenium having characteristics of higher polarizability, the resulting compound of tetramethyltetraselenafulvalene (TMTSF) exhibited many phenomena of superconductivity.[11,17−19] It was interesting to note that a small structural modification at side groups of TMTSF leading to the corresponding hexamethylenetetraselenafulvalene (HMTSF)[20] resulted in the loss of superconductivity characteristics. However, HMTSF remaining as an important conducting organic donor molecule similar to those derivatives mentioned above. They continue to play an important role in the development of molecular electron-transporting materials and superconductors.[21]

The main electronic aspect of the current study is to demonstrate high efficiency in photoinduced intramolecular and intermolecular electron (e⁻)-transfer mechanisms between conducting organic electron donors and electron-accepting fullerenes for the dielectric enhancement. The property change arises from the formation of charge-polarization states among layers of nanoparticles under photoactivation. One molecular example of intramolecular phenomena was given by the covalently fused dumbbell triad C_{60}−TTF−C_{60} conjugate.[22] The study was performed by using picosecond transient absorption measurements to detect directly several nanosecond transient bands in the spectrum corresponding to optical absorptions of cationic TTF radical and anionic [60]fullerene

radical (λ_{abs} 1060 nm) moieties of a CS structure as C_{60}−TTF⁺•−C_{60}⁻•, giving the evidence of e⁻ transfer. Related many intermolecular e⁻-transfer systems involving C_{60}- and TTF-derived donor analogous mixtures were often used in the study of photoenergy conversion to produce electricity.[23]

As the refractive index value of a given medium is dependent on the dielectric constant or relative permittivity (ε_r) in response to incident electromagnetic (EM) waves, it is plausible to alter both the refractivity and reflectivity of EM waves at the surface of the medium by tuning and regulating its dielectric characteristics. In term, this dielectric parameter can be modulated by the change of material's e⁻ polarization in the medium. Therefore, it is reasonable to propose the use of highly electron-donating organic donors, such as TTF derivatives, as the source of electron supply to increase the number of separated charges in the photoresponsive dielectric medium. The approach can be coupled with our recent synthesis of plasmonic trilayered (γ-FeO_x@AuNP) @$[C_{60}(>DPAF-C_9)_x]_n$ NPs[8] for the comparison of photoswitchable dielectric property enhancement by the additional amplification effect contributed from noncovalently attached conducting electron donors. We assume that stronger electron-donating ability of TTF derivatives than that of light-harvesting DPAF-C_9 antenna may allow dual contributions from both types of organic donors, where DPAF-C_9 serves as a photoresponsive e⁻ donor to initiate the intramolecular photoinduced e⁻ transfer to C_{60}> cage with the formation of (DPAF)⁺•-C_9 cation radical as the first step. This photoprocess can then be followed by the intermolecular e⁻ transfer from TTF derivatives to (DPAF)⁺•-C_9 forming neutral DPAF-C_9 and (TTF)⁺• that results essentially in moving the cationic charges into the outer layer of nanospherical particle. The photomechanism becomes the fundamental e⁻ polarization process for the amplification of dielectric properties.

■ EXPERIMENTAL SECTION

Preparation of rf-Responsive Multilayered Core−Shell Nanoparticles. Synthesis of γ-FeO_x and the plasmonic metallic gold-coated γ-FeO_x@AuNP nanoparticles followed a similar procedure reported previously.[2] Because there was a slight variation of the particle size, layer thickness, and yield in each batch of the reaction, a large scale preparation was carried out and applied for the subsequent step synthesis of trilayered and tetralayered core−shell NPs. This ensured the consistency

of γ-FeO$_x$@AuNP characteristics by using the same batch of materials. Spectroscopy data: FT-IR (KBr) ν_{max}: 2956 (w), 2918 (m), 2846 (m), 1588 (s), 1399 (s), 1261 (w), 1089 (w), 1016 (w), 970 (w), 905 (w), 810 (m), and 580 (vs) cm^{-1}.

Preparation of C$_{60}$(>DPAF-C$_9$) (1-C$_9$)-Encapsulated γ-FeO$_x$@AuNP Yielding Trilayered Core—Shell Nanoparticles, (γ-FeO$_x$@AuNP)@[C$_{60}$(>DPAF-C$_9$)]$_n$ (11-NPs). The preparation method followed the procedure reported previously[2] with slight modification of reaction conditions. The material weight ratio between γ-FeO$_x$@AuNP and **1**-C$_9$ used was maintained in a relatively similar range for easy comparison of spectroscopy and physical property data with those reported previously. Spectroscopy data of **11**-NPs were given in the Supporting Information.

Deposition of Electron Donors onto (γ-FeO$_x$@AuNP) @[C$_{60}$(>DPAF-C$_9$)]$_n$ To Yield the Corresponding 12-NPs, and 15-NPs to 21-NPs. Both (γ-FeO$_x$@AuNP) @[C$_{60}$(>DPAF-C$_9$)]$_n$ (**11**-NPs, 150 mg) and one of the electron donors, as shown in Figure 1, in a predefined amount, for example, to match with a calculated molar ratio of C$_{60}$>/e$^-$ donor as either 1:1, 1:2, 1:5, or 1:10 were dissolved in toluene (40 mL) under ultrasonication for a period of more than 1.0 h until a homogeneous nanoparticle dispersion was obtained. The solution was concentrated via rotary evaporation to a volume of <3.0 mL. At this concentration, the molecular contact of **11**-NPs to electron-donor molecules was largely increased. Resulting encapsulated magnetic nanoparticles were physically removed from the container solution using an external permanent magnet. The process excluded a residual amount of **1**-C$_9$ remaining in the solution. Collected magnetic nanoparticles were washed repeatedly by ethanol and diethyl ether in sequence to furtherly remove residual donor molecules from the nanoparticle surface. It was followed by drying in vacuo to afford dark brown solids. Spectroscopy data of tetralayered (γ-FeO$_x$@AuNP)@[C$_{60}$(>DPAF-C$_9$)]$_n$@(TMTTF)$_m$ (**12**-NPs) and (**11**-NPs)@(TMSeTTF)$_m$ (**15**-NPs) were given in the Supporting Information.

Instrumentation and Spectroscopy Measurements. Cyclic voltammetry (CV) was recorded on an EG&G Princeton Applied Research 263A potentiostat/galvanostat. Cyclic voltammograms of several electron donors were collected at different voltages versus Ag/Ag$^+$ using Pt as the working and counter electrodes and Ag/AgCl as the reference electrode at a scan rate of 10 mV/s. A solution in a concentration of 1.0×10^{-3} M in CH$_3$CN—CH$_2$Cl$_2$ containing the electrolyte (n-butyl)$_4$N$^+$—PF$_6^-$ (0.2 M) was used for all CV measurements.

^{1}H NMR and ^{13}C NMR spectra were recorded on either a Bruker AVANCE Spectrospin-200 or Bruker AC-300 spectrometer. UV—vis spectra were recorded on a Hitachi U-3410 UV spectrometer. Infrared spectra were recorded as KBr pellets on a Nicolet 750 series FT-IR spectrometer.

Energy-dispersive X-ray spectroscopy (EDS) was recorded on the JEOL JSM 7401F field-emission scanning electron microscope equipped with an EDAX Genesis XM2 imaging system which consists of a 10 mm^2 Si(Li) detector with a SUTW window for the detection of all elements down to Be atom. The system is also equipped with the digital electronics and software for image acquisition and X-ray signal mapping, with qualitative and quantitative analysis capabilities. Transmission electron microscopy (TEM) measurements were carried out on a Philips EM400T transmission electron microscope. In the sample preparation for the collection of

TEM micrographs, a carbon—copper film grid in a 200-mesh size was used as the supporting plate for directly coating of a nanoparticle sample in a solution of 1.0×10^{-6} M on the grid. All solvents were removed and dried by the freeze—dry technique to prevent the solvent removal-induced particle aggregation.

Measurements of Dielectric Properties in Terms of Permittivity or Relative Dielectric Constant (ε'_r). Dielectric property measurements were carried out by an Agilent Network Analyzer (Agilent Technologies, Inc., Santa Clara, CA, USA) equipped with an open-ended Agilent 85070E dielectric probe kit in a detection range of 200 MHz to 50 GHz. We conducted the system base-line calibration by using open-ended, close-ended, and attenuated calibrators prior to each measurement to ensure the removal of instability, induced by the cable connection, and system drift errors. In the experiment, a complex scattering parameter, defined as S_{11}, was measured and converted to relative complex electric dielectric constant values using Agilent 85071E Materials Measurement Software. This complex form consists of both real and imaginary parts. The former term represents the value of dielectric constant, and the latter is defined as the loss factor.

The light source used in the measurement included a collimated white light-emitting diode (LED) light with an output power of 2.0 W (Prizmatix, USA). All permittivity measurements were performed in a custom-built chamber that was conducted under a circumferentially uniform illumination environment. The uniformness was achieved by the installation of a reflective half-circular aluminum plate at the back-wall side surrounding the testing tube which was located at the center of the chamber. A LED light beam was allowed to pass through a small window opening at the front side of the chamber for the sample irradiation. Some reflected light beams were designed to refocus from the back-side aluminum mirror plate back to the sample-containing tube. We installed four small fans with two at the top and one at each side wall of the chamber to control and prevent the temperature increase inside the chamber during the experiment. The illumination period was fixed at 60 min. A poly(dimethylsiloxane) (PDMS, 1.0 g) semisolid was applied as a polymer matrix host which is capable of forming a pastelike material sample in mixing with a predefined quantity of nanoparticles. In a typical preparation, a mixture of PDMS and one of several rf-responsive core—shell nanoparticle materials (100 mg) was blended by dissolving both components in ethyl acetate (20 mL) in a testing tube under sonication. It was followed by solvent evaporation to yield pastelike semisolid materials filling in the tube.

RESULTS AND DISCUSSION

Design and Preparation of Electron Donors and Multilayered Nanospherical Particles. One of the most unique electronic characters of a fullerene cage is its high electronegativity associated with the unusually strong e$^-$-accepting ability to oxidize organic donor molecules or polymers. Electron transfer from a strong to moderate e$^-$ donor to C$_{60}$ can occur instantaneously upon contact. In the presence of a weak donor, the e$^-$ transfer can be induced under the condition of photoactivation.[24] Mechanisms of photo-induced e$^-$-transfer reactions involving C$_{60}$, C$_{70}$, or higher fullerenes in mixture components have been investigated extensively by photochemical techniques, such as laser flash photolysis or pulse-radiolysis studies.[25—28] It was evident that the formation of C$_{60}^{-\bullet}$ and C$_{70}^{-\bullet}$ was usually produced via their
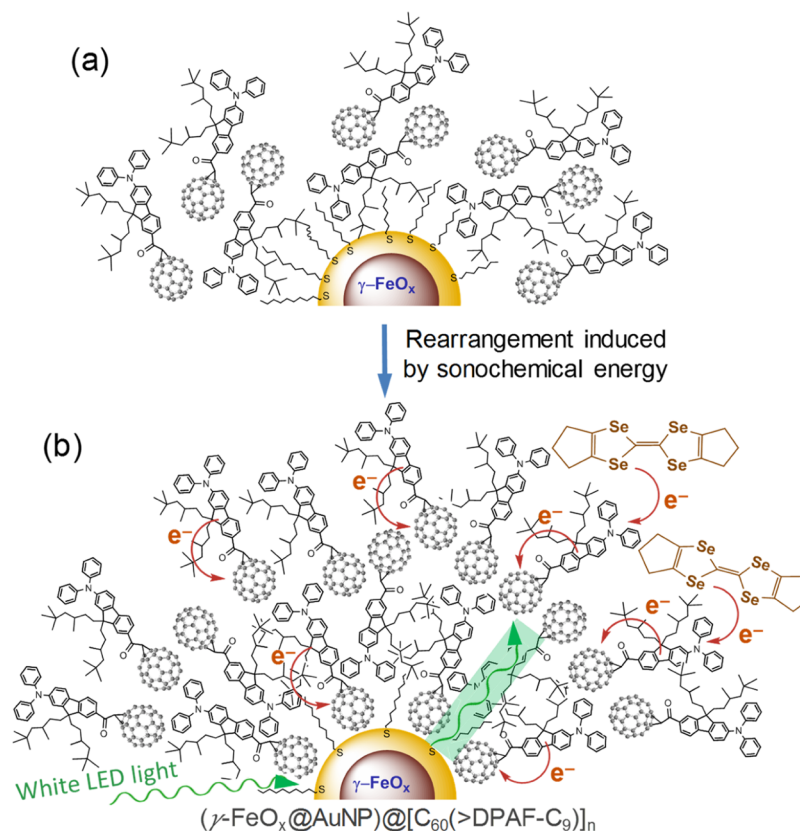
Figure 2. Schematic description of rf-responsive multilayered core−shell nanoparticle construction of (a) initial deposition of **1**-C$_9$ on bilayered γ-FeO$_x$@AuNPs and (b) rearrangement of **1**-C$_9$ to form partial bilayered [60]fullerosome as **11**-NPs, followed by the deposition of e$^−$ donors HMTSF to form **18**-NPs. Plasmonic energy (green rectangle shadow)-induced intramolecular and intermolecular electron-transfer mechanisms were indicated.

triplet states (^{3}C$_{60}^*$ or ^{3}C$_{70}^*$) using short wavelengths, such as common UVA light (350−400 nm), which then abstract one electron from an e$^−$-donor molecule or moiety present in the vicinity. In the case of a molecular system having covalently bound C$_{60}$-donor chromophore antenna conjugates exhibiting high extinction coefficient at visible wavelengths, photoinduced e$^−$ transfer may also take place via the singlet state of the e$^−$-donor chromophore using long photoexcitation wavelengths (>400 nm) where the C$_{60}$ cage is weak in optical absorption.[29,30] These charged transient states were differentiated and determined easily by the corresponding transient optical absorption showing much shifted from those of the ground state. Long-lived CS states were achieved by enhancing redox properties of the donor, tuning the distance between the donor−acceptor pair and/or increasing the degree of intramolecular charge resonance.[4] All of these effects were adopted as the basic parameters of material variation for the current investigation aimed to create a distinguishable electron-polarizable dielectric medium upon photoexcitation. By taking the advantage of electron-conducting capability of stacked TTF derivatives and π-conjugated poly(alkylthiophene) used in the fabrication of photovoltaics with C$_{60}$ monoadducts,[31,32] the internally produced e$^−$ polarization leading to the detectable photocurrent being induced may provide the appropriate mechanism for the design of dielectric enhancement and guide the goal to achieve permittivity (ε_r') amplification using our core−shell nanoparticle systems.

To make the direct comparison of measured relative dielectric constants with our previous reports,[1,2] we applied the same covalently bound e$^−$-donating chromophore 9,9-di(3,5,5-trimethylhexyl)-2-diphenylaminofluorene (DPAF-C$_9$) attached on a C$_{60}$ forming methano[60]fullerene dyad of C$_{60}$(>DPAF-C$_9$) (**1**-C$_9$, Figure 1) in the study. High-molecular e$^−$-polarizability characteristics were substantiated recently in **1**-C$_9$ upon photoexcitation.[33] The molecular structure of **1**-C$_9$ consists of an electronically polarizable push−pull conjugation having the DPAF-C$_9$ arm working as the push moiety to result a positively charged (DPAF)$^{+\bullet}$-C$_9$, whereas the C$_{60}$> cage serves as the corresponding pull moiety to afford a negatively charged (C$_{60}$>)$^{-\bullet}$. The separation distance between these two moieties is only ∼3.5 Å, as determined by the X-ray crystal structure of a similar conjugation.[34] The associated periconjugation between C$_{60}$> and the carbonyl moiety of DPAF-C$_9$ with the concurrence of keto−enol tautomerism[8] at the conjugation bridge was reasoned for the facile ultrafast photoinduced intramolecular e$^−$-transfer rate in femtoseconds.[34] By adding stronger TTF-derived e$^−$ donors on top of the DPAF-C$_9$ layer in the plasmonic partial bilayer [60]fullerosome-based nanoparticle construction (Figure 2), we propose that the initially formed CS state (C$_{60}$>)$^{-\bullet}$[>(DPAF)$^{+\bullet}$-C$_9$] may further induce the subsequent e$^−$ transfer from TTF derivatives to neutralize (DPAF)$^{+\bullet}$ moiety to generate the secondary CS state of (C$_{60}$>)$^{-\bullet}$[>(DPAF)-C$_9$]−TTF$^{+\bullet}$. Additional electron transfer from another TTF molecule to C$_{60}$> is also possible to result in a higher charge state of (C$_{60}$>)$^{-2}$[>(DPAF)-C$_9$]−(TTF$^{+\bullet}$)$_2$. All of these events should enhance dielectric properties of the nanoparticle medium.

We selected several TTF (**2**) derivatives, such as 2,3,6,7-tetramethyltetrathiafulvalene (TMTTF, **3**), 2,3,6,7-tetrakis-(methylseleno)tetrathiafulvalene (TMSeTTF, **4**), 2,3,6,7-tetrakis (phenylseleno)tetrathiafulvalene (TPSeTTF, **5**), BEDT-TTF (**6**), and HMTSF (**7**), as shown in Figure 1, for the study. New compounds **4** and **5** were synthesized according to the reported methods[35−40] by a modified procedure. In the current synthesis, the key intermediate tetraanionic TTF (TTF^{-4}) was generated by the use of lithium diisopropylamide (4.0 equiv) at −78 °C prior to the addition of either dimethyldiselenide (CH$_3$Se−SeCH$_3$) or diphenyldiselenide (PhSe−SePh) for the preparation of compounds **4** or **5**, respectively, in a yield of 75%. Alternatively, TTF^{-4} can be quenched by selenium powder (4.0 equiv) at −78 °C to give the corresponding intermediate of TTF−(Se$^-$)$_4$, followed by the reaction with methyliodide at ambient temperature to obtain **4** in a yield of 80%. Because both **4** and **5** are symmetrical in the molecular structure, spectroscopy characterization by ^{1}H NMR spectrum (CDCl$_3$) was relatively simple, showing a singlet proton peak at δ 2.34 for the compound **4** and two groups of aromatic protons centered at δ 7.31−7.25 (m, 3H) and 7.52−7.49 (m, 2H) for the compound **5**. Synthetic procedure and the spectroscopy data were given in the Supporting Information.

To construct rf-responsive multilayered nanomaterials, we began with the fabrication of bilayered core−shell nanoparticles γ-FeO$_x$@AuNP with the plasmonic gold layer located at the outer shell. The synthesis of magnetic γ-FeO$_x$ nanoparticles was carried out by the thermolysis of oleic acid−Fe^{+3} complex salt [iron(III) oleate] at 320 °C to afford monodisperse nanocrystals. The surface of these particles was stabilized by excessive oleic acid in situ that rendered its solubility in organic solvents. To make the deposition of hydrogen tetrachloroaurate(III) trihydrate (HAuCl$_4$·3H$_2$O) possible, the surface of γ-FeO$_x$ NPs was first modified with the second layer of oleic acid that resulted in the orientation of many acid groups (−CO$_2$H) being positioned at the outer layer of the particle facing to the solvent. This facilitated the subsequent salt exchange with (CH$_3$)$_4$N$^+$−OH$^-$ in H$_2$O leading to high water solubility of resulting nanoparticles. Neutralization of HAuCl$_4$ by the surface base (OH$^-$) gave the smooth deposition of crystalline gold nanoparticles after reduction in the presence of sodium citrate dihydrate and hydroxylamine hydrochloride. Resulting NPs were stabilized by the addition of 1-octanethiol, as a binding and capping agents, in toluene forming organic solvent-soluble γ-FeO$_x$@AuNPs. They were removed easily from the solution by an external magnet and purified. Other related preparation methods of monodispersed nanocrystals based on starlike copolymer templates as nanoreactors were reported recently[41−45] that provided alternative approaches to control the particle size.

Encapsulation of γ-FeO$_x$@AuNPs by C$_{60}$(>DPAF-C$_9$) (**1**-C$_9$) to the formation of trilayered core−shell NPs (Figure 2) was performed under ultrasonication using the preformed bilayer structure. Because all encapsulated magnetic nanoparticles were physically removed from the container solution with the assistance of an external permanent magnet and washed repeatedly by ethanol and diethyl ether, we were able to ensure the products being free from residual nonbinding **1**-C$_9$ molecules at the surface. The initial binding force was governed by the strong hydrophobic−hydrophobic interactions among (C$_{60}$>)−(C$_{60}$>) cages to form a layer membrane of partial bilayer [60]fullerosome (Figure 2a) as those reported.[46] Regarding the subsequent orientation of **1**-C$_9$ at the surface

under ultrasonication conditions, we proposed that the strong binding interaction forces of C$_{60}$> cages to the gold surface[47−49] should lead to the partial replacement of 1-octanethiol capping molecules via alkylthiol ligand−C$_{60}$> exchange, induced by sonochemical energy to invert **1**-C$_9$ molecules. The exchange should form a monolayer of C$_{60}$(>DPAF-C$_9$) with the orientation of DPAF-C$_9$ moiety facing outward from the gold surface,[50] as shown in Figure 2b. This orientation is also consistent with the fact that the calculated surface binding energy of C$_{60}$−Au was found to be higher than the bond strength of Au−S.[51] Subsequent packing of the second C$_{60}$(>DPAF-C$_9$) layer at the surface should also follow the same strong hydrophobic−hydrophobic interaction forces of (C$_{60}$>)−(C$_{60}$>) cages that resulted in a molecular self-assembly of **1**-C$_9$ conjugates to form a partial bilayered [60]fullerosome configuration with the DPAF-C$_9$ moiety orientation facing outward. This is the proposed nanostructure of trilayered (γ-FeO$_x$@AuNP)@[C$_{60}$(>DPAF-C$_9$)]$_n$ as **11**-NPs without HMTSF molecules in Figure 2b.

Deposition of the fourth layer of TMTTF analogous e$^-$-donor molecules onto **11**-NPs was carried out with a calculated molar ratio of C$_{60}$>/TMTTF as either 1:1, 1:2, 1:5, or 1:10 in a concentrated solution of toluene under the condition of ultrasonication, followed by the physical removal of resulting encapsulated magnetic nanoparticles from the container solution using an external permanent magnet to afford dark brown solids of tetralayered (γ-FeO$_x$@AuNP)@[C$_{60}$(>DPAF-C$_9$)]$_n$@(TMTTF)$_m$ (**12**-NPs). Similar procedures were used to prepare several related nanoparticles of (**11**-NPs) @(TMSeTTF)$_m$ (**15**-NPs), (**11**-NPs)@(TPSeTTF)$_m$ (**16**-NPs), and (**11**-NPs)@(HMTSF)$_m$ (**18**-NPs) with the schematic core−shell nanoparticle configuration shown in Figure 2b and used in the permittivity investigation below.

Characterizations of Core−Shell rf-Responsive Nanomaterials. Verification of a core−shell structural configuration for all nanospherical particles was performed using TEM micrographs. It included morphology and topography investigations of all NPs to show the core and shell thicknesses of trilayered **11**-NPs (Figure 3C), tetralayered **12**-NPs [(**11**-NPs) @(TMTTF)$_m$, Figure 3D], and tetralayered **18**-NPs [(**11**-NPs) @(HMTSF)$_m$, Figure 3E] by sequential layer depositions. Average size of the parent γ-FeO$_x$ nanoparticles (Figure 3B) was measured to be small as 8.0−10 nm in diameter in a roughly homogeneous narrow distribution. Deposition of a gold layer on the surface of γ-FeO$_x$ NPs to a structure of γ-FeO$_x$@AuNP was controlled to a shell thickness of <∼8.0 nm by the calculated quantity of HAuCl$_4$ applied, assuming its chemical reduction produced the same weight amount of solid nanocrystals. We used the contrast difference to indicate a darker core iron oxide particle region with a slightly lighter gold shell to estimate the gold shell thickness of roughly 3.0−5.0 nm. With an additional layer of C$_{60}$(>DPAF-C$_9$)-derived fullerosome capping, the average particle size of **11**-NPs increased to roughly 20 nm in diameter (Figure 3C) in an approximately homogeneous narrow distribution. This corresponds to an estimated [60]fullerosome layer thickness of ∼6.0−8.0 nm, matching well with a bilayered to partial trilayered molecular width of C$_{60}$(>DPAF-C$_9$) (molecular long-axis length of ∼3.2 nm), consistent with the schematic layer configuration of Figure 2b. Further deposition of the e$^-$-donor TMTTF or HMTSF molecules in a C$_{60}$>/e$^-$-donor molar ratio of 1:5 onto **11**-NPs gave the corresponding TEM micrographs (Figure 3D or 3E, respectively), showing a layer of organic substance in a
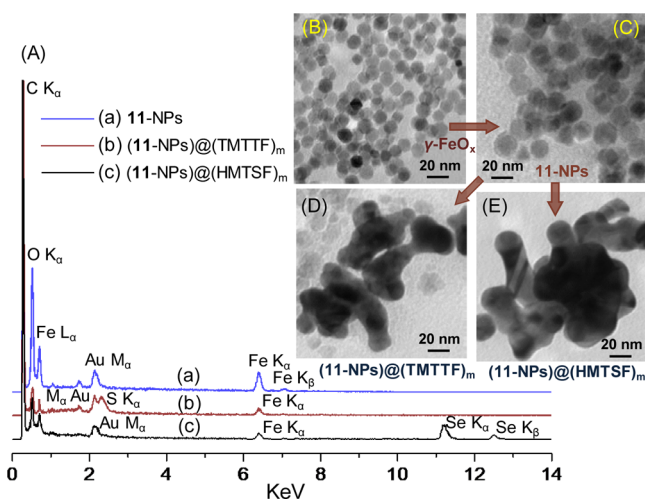
Figure 3. (A) Energy-dispersive spectrum (EDS) of (a) trilayered (γ-FeO$_x$@AuNP)@[C$_{60}$(>DPAF-C$_9$)$_x$]$_n$ (**11**-NPs), (b) tetralayered (**11**-NPs)@(TMTTF)$_m$ (**12**-NPs), and (c) tetralayered (**11**-NPs)@(HMTSF)$_m$ (**18**-NPs), showing the corresponding atomic compositions where some carbon contents may arise from the background tape used for sample holding at the surface. The oxygen content peak was from both the sample and the environment. TEM micrograph images of (B) γ-FeO$_x$ NPs, (C) **11**-NPs, (D) **12**-NPs, and (E) (γ-FeO$_x$@AuNP)@[C$_{60}$(>DPAF-C$_9$)]$_n$@(HMTSF)$_m$ (**18**-NPs).
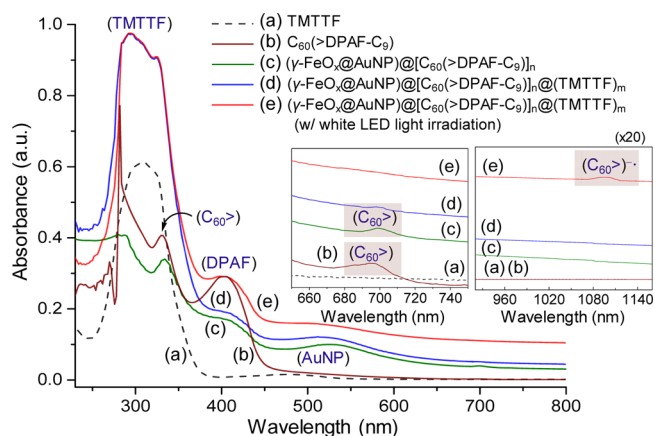
Figure 4. Steady-state UV−vis absorption of (a) TMTTF, (b) **1**-C$_9$, and multilayered core−shell nanoparticles (c) **11**-NPs and (d) **12**-NPs in the absence of external light exposure. (e) **12**-NPs under external white LED light irradiation. All samples were prepared in CHCl$_3$−THF (1:5) with the concentration of 1.0×10^{-5} M.

soft amorphous contrast image covering over multiple particles. We estimated the average width of dark non-overlapped shell regions to indicate an increase in particle diameter to roughly 25−30 nm.

We applied microanalyses of energy-dispersive X-ray spectra (EDS) of all NPs to confirm their elemental composition. It was carried out on a cluster sample of **11**-NPs, **12**-NPs, and **18**-NPs deposited on a supporting tape, as examples. The latter two samples were prepared by a C$_{60}$>/(TMTTF or HMTSF) molar ratio of 1:5. As a result, the atomic percentages of carbon, Fe, and Au of **11**-NPs were measured to be 57.12, 16.08, and 1.13%, respectively (Figure 3Aa), giving an atomic C/Fe/Au ratio of 50.6:14.2:1.0, revealing a thin layer of gold nanocrystals. By using this ratio as the reference, the atomic C/Fe/Au/S percentage of tetralayered **12**-NPs (Figure 3Ab) and the C/Fe/Au/Se percentage of tetralayered **18**-NPs (Figure 3Ac) were measured to be 60.74:6.45:0.64:19.89 and 62.79:6.67:0.55:19.57, respectively, indicating the elemental contribution of TMTTF or HMTSF dominating the EDS data. Perhaps, it is owing to the fact that EDS measurements were based on the surface evaluation giving a prominent contribution on molecules located at and nearby the surface region. In the elemental analysis of **12**-NPs, because we prepared the sample based on a 5.0 equiv ratio of TMTTF molecules versus one C$_{60}$> cage, we used an equivalent of 20 sulfur atoms as the unit for a 19.89% EDS value in calculation to reach a value of 49.7% of carbon on TMTTF molecules alone. The detected additional 11.04% carbon should be raised from C$_{60}$(>DPAF-C$_9$) conjugates located underneath the TMTTF layer. Similarly, EDS measurement only exhibited less than a half atomic percentage of Fe and Au as compared with those of **11**-NPs. In the case of **18**-NPs, a very similar C/Fe/Au/Se percent ratio was obtained implying the successful deposition of a 5.0 equiv ratio of HMTSF molecules versus one C$_{60}$> cage on **11**-NPs.

Steady-state optical absorption of C$_{60}$(>DPAF-C$_9$) (Figure 4b) was dominated by two chromophore components of the

C$_{60}$> cage moiety centered at 332 nm (λ_{max}, $\varepsilon = 4.06 \times 10^4$ L mol^{-1} cm^{-1}) and the DPAF moiety at 412 nm (λ_{max}, $\varepsilon = 2.90 \times 10^4$ L mol^{-1} cm^{-1}). The latter serves as a light-harvesting antenna when either UVA or white LED light is applied for the photoactivation. Its absorption band was overlapped partially with the broad optical absorption of AuNP subshell layer covering over the full spectrum wavelengths with the maximum band peak (λ_{max}) centered at 540 nm (Figure 4c) that made the interlayer energy transfer efficient. Both optical absorptions are crucial for this study that allows us to execute and achieve photoinduced SPR energy generation at these wavelengths (300−600 nm). Accumulated SPR energy is transferrable from the inner Au shell layer to the outer C$_{60}$(>DPAF-C$_9$)-derived fullerosome layer (Figure 2b) to effect the intramolecular charge transfer of **1**-C$_9$, resulting in the generation of CS transient state C$_{60}{}^{-\bullet}$(>DPAF$^{+\bullet}$-C$_9$). Interestingly, we were able to detect a weak absorption band centered at 1090 nm (the second inset of Figure 4e) corresponding to that of the (C$_{60}$>)$^{-\bullet}$ moiety under the white LED light irradiation while collecting the UV−vis spectrum simultaneously. This new [60]fullerenyl anion radical absorption band was red shifted from the 670−700 nm band (the first inset of Figure 4b,c) of the C$_{60}$> cage moiety. Detection of the weak 1090 nm band in the presence of TMTTF donors, located at the most outer shell layer, was crucial because it clearly revealed the occurrence of the secondary e$^-$ transfer directly or indirectly (via DPAF$^{+\bullet}$) from TMTTF moieties to C$_{60}$> upon external photoexcitation. Because optical absorption of the TMTTF moiety was only detectable at λ_{max} 315 nm ($\varepsilon = 6.10 \times 10^4$ L mol^{-1} cm^{-1}), it should not be considered as the moiety subjected to photoexcitation using a white light. In addition, the main absorption (λ_{max}) of C$_{60}$> moiety also occurs at 332 nm (Figure 4b), it was not considered for photoexcitation either. Accordingly, we proposed a plausible pathway involving initial photooxidation of the DPAF-C$_9$ moiety at 412 nm (λ_{max}, Figure 4e), followed by the induced secondary e$^-$ transfer from the outer TMTTF molecules of tetralayered (γ-FeO$_x$@AuNP)@[C$_{60}{}^{-\bullet}$(>DPAF$^{+\bullet}$-C$_9$)]$_n$@(TMTTF)$_m$ (**13**-NPs) to the inner DPAF$^{+\bullet}$-C$_9$ moiety forming a new CS state of (γ-FeO$_x$@AuNP)@[C$_{60}{}^{-\bullet}$(>DPAF-C$_9$)]$_n$@(TMTTF$^{+\bullet}$)$_m$ (**14**-NPs). Owing to a slightly larger separation distance between TMTTF and C$_{60}$> moieties at solid layers, the charge

recombination rate could be slowed down significantly to allow us detecting the 1090 nm band. Furthermore, absorption intensity of photoexcited **14**-NPs (Figure 4e) was found to increase progressively toward longer wavelengths as compared with those of neutral **12**-NPs (Figure 4d). It may also be indicative of additional absorptions contributed from that of $(TMTTF)^{+\bullet}$ at 680−760 nm (estimated) consistent with those (750−1100 nm) reported for the radical pair of $(C_{60}^{-\bullet})−(TTF^{+\bullet})$.[25]

To investigate the redox potential difference among various e^- donors in interactions with $C_{60}>$, we carried out the CV measurements of TMTTF (**3**), TMSeTTF (**4**), TPSeTTF (**5**), and a mixture of $C_{60}(>DPAF-C_9)$ and TMTTF in $CH_2Cl_2−CH_3CN$. They were performed in the presence of $(n-butyl)_4N^+−PF_6^-$ electrolyte using Pt as working and counter electrodes and Ag/AgCl as the reference electrode. The CV characteristics of compounds **3**−**5** under variation of the cyclic. Oxidation voltage versus Ag/Ag$^+$ from −2.0 to 1.8 V were evaluated, as shown in Figure 5a. It displayed two consistent
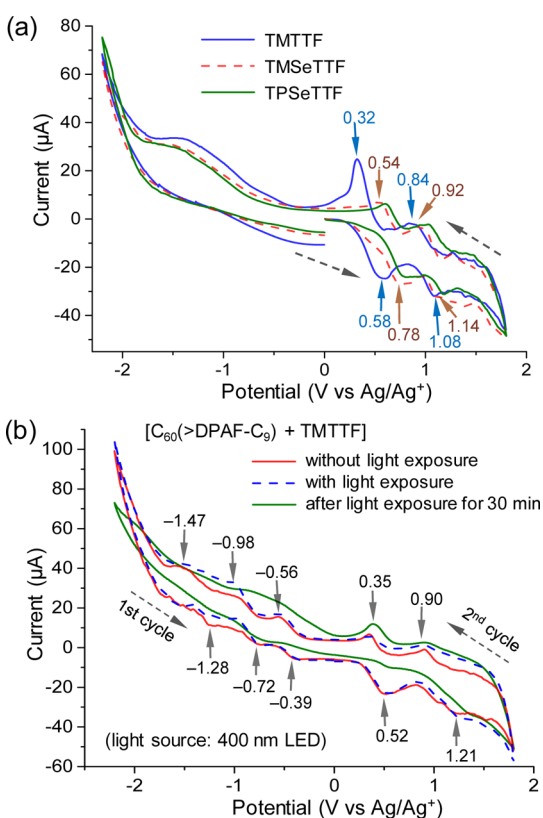
Table 1. Cyclic Voltammetry Data of the First and Second Oxidation−Reduction Potentials (V) vs Ag/Ag$^+$

e^--donor	$^1E_{ox}$	$^1E_{red}$	$^1E_{1/2}$	$^2E_{ox}$	$^2E_{red}$	$^2E_{1/2}$	$\Delta E_{1/2}$
TMTTF	0.32	0.58	0.45	0.84	1.08	0.96	0.51
TMSeTTF	0.54	0.78	0.66	0.92	1.14	1.03	0.37
TPSeTTF	0.59	0.79	0.69	1.02	1.18	1.10	0.41
BEDT-TTF	0.56	0.73	0.65	0.95	1.21	1.08	0.43
HMTSF	0.56	0.72	0.64	1.01	1.17	1.09	0.45

analogous were deviated from each other with the higher potentials for **4** or **5** having the attachment of alkyl- or phenyl-seleno side groups, respectively, instead of four simple methyl groups in TMTTF. By using the first oxidation−reduction potentials $(^1E_{ox}/^1E_{red})$ of TMTTF as the reference, we evaluated the influence of donor's redox potentials in the presence of a strong $C_{60}>$ acceptor in solution. In the absence of light exposure, Figure 5b (the red line) displayed the $^1E_{ox}/^1E_{red}$ and $^2E_{ox}/^2E_{red}$ values in the oxidation wave of the mixture of **1**-C$_9$ and TMTTF as 0.32/0.52 and 0.90/1.21 V versus Ag/Ag$^+$, respectively, being similar to those of TMTTF alone. This revealed that the one-electron oxidation process of a weaker DPAF-C$_9$ donor moiety in the structure of **1**-C$_9$ having a much higher $^1E_{ox}$ value[52] of 0.82 V versus Ag/Ag$^+$ was overshadowed by the facile electron oxidation of the stronger TMTTF donor. Fullerenes are highly electronegative cages. It is capable of accepting multiple electrons easily in consecutive reductions to exhibit, commonly, at least three reversible redox waves, showing $^1E_{red}/^1E_{ox}$, $^2E_{red}/^2E_{ox}$, and $^3E_{red}/^3E_{ox}$ potential values as −0.39/−0.56, −0.72/−0.98, and −1.28/−1.47 V versus Ag/Ag$^+$ (Figure 5b), respectively. Most importantly, in the presence of the white LED light irradiation while collecting the CV voltammograms, we found that all oxidation and reduction potential values (the dashed blue line of Figure 5b) at the initial stage were basically unchanged. However, while allowing the irradiation to continue for a period of 30 min, we detected significant changes of the most of oxidation−reduction potentials in the cyclic waves with the loss of main features at each redox cycle, except the first oxidation potential ($^1E_{ox}$, the solid blue line of Figure 5b). The observation clearly implied the occurrence of photoinduced intermolecular e^- transfer directly or indirectly from TMTTF to $C_{60}>$ forming the corresponding $(TMTTF)^{+\bullet}$ or $(TMTTF)^{2+}$ and $(C_{60}>)^{-\bullet}$ or $(C_{60}>)^{-n}$ ($n \leq 3$) moieties that prohibited further oxidation waves of these ions and/or radical pairs. The CV results may be correlated with or indicative of similar charge polarization phenomena to occur in the solid state of tetralayered **12**-NPs.

Permittivity and Dielectric Investigations of rf-Responsive Nanomaterials. Our main objective of this study is to investigate the role of electron donors in enhancing the dielectric properties of a nanoparticle medium for microwave applications. In the nanomaterial's design, we applied photoinduced SPR energy to cause intramolecular e^- polarization of $C_{60}(>DPAF-C_9)$ that coupled with intermolecular e^- transfer from TTF derivatives within the multilayered configuration of nanoconjugates. To achieve the near-field effect during the plasmon energy-transfer event between photoexcited Au NPs and $C_{60}(>DPAF-C_9)$, we assembled a four-layered core−shell structure of nanospherical particles with a thin AuNP shell beneath the **1**-C$_9$ shell in direct contact. All components other than the γ-FeO$_x$ core were able to absorb light energy for photoexcitation at different wavelength ranges. The amount of LED light photons to be captivated at the

Figure 5. Cyclic voltammograms (CV) of (a) three electron donors indicated and (b) a mixture of $C_{60}(>DPAF-C_9)$ and TMTTF at different voltages versus Ag/Ag$^+$ in a solution concentration of 1.0×10^{-3} M in $CH_3CN−CH_2Cl_2$, containing $(n-butyl)_4N^+−PF_6^-$ electrolyte (0.2 M), using Pt as working and counter electrodes and Ag/AgCl as the reference electrode at a scan rate of 10 mV/s.

reversible oxidation−reduction cycle waves for each compound with the first $(^1E_{ox}/^1E_{red})$ and second $(^2E_{ox}/^2E_{red})$ oxidation−reduction potentials at the current maximum/minimum values measured for **3**, **4**, and **5** as 0.32/0.58 and 0.84/1.08, 054/0.78, and 0.92/1.14, and 0.59/0.79 and 1.02/1.18 V versus Ag/Ag$^+$ (Table 1, including those of BEDT-TTF and HMTSF), respectively. It is interesting to note that the first $(^1E_{1/2})$ and second $(^2E_{1/2})$ half-wave potentials of the similar TTF

surface was dependent on the shape morphology, particle size, and thickness of the AuNP layer. It also relied on the quantity of e$^-$ donors exhibiting absorption wavelengths in overlap with the emission wavelength and intensity of the white LED light at 400−600 nm. Therefore, to ensure the consistency of experimental results, we prepared the basic core−shell nanoparticles of $(\gamma\text{-FeO}_x@\text{AuNP})@[\text{C}_{60}(>\text{DPAF-C}_9)_x]_n$ (**11-NPs**) in a large scale and used the same batch for each sample preparation of tetralayered $(\gamma\text{-FeO}_x@\text{AuNP})@[\text{C}_{60}(>\text{DPAF-C}_9)]_n@(\text{TMTTF})_m$ (**12-NPs**) analogous with a variation of different e$^-$ donors. We denoted the tetralayered core−shell NP samples derived from TMSeTTF [as (**11-NPs**) @$(\text{TMSeTTF})_m$ or **15-NPs**], TPSeTTF (**16-NPs**), BEDT-TTF (**17-NPs**), HMTSF (**18-NPs**), P3HT (**19-NPs**), PANi (**20-NPs**), and PANi-CSA (**21-NPs**) as the sample symbol indicated in parenthesis (Figure 1).

We separated all samples into two groups in the frequency-dependent relative dielectric constant (ε'_r) or permittivity measurements. The first group included the encapsulation deposition of similar molecular e$^-$ donors as **12-NPs**, **15-NPs**, **16-NPs**, **17-NPs**, and **18-NPs**. The second group composed of e$^-$-conducting polymers to be at the most outer shell layer of **19-NPs**, **20-NPs**, and **21-NPs**, using the sample of BEDT-TTF-derived **17-NPs** as the reference for comparison. Soft elastic PDMS was used as a polymer host to provide a tight packing and air-gap filling among nanospherical particles after solvent evaporation. It is critical for eliminating the air contribution to the measured ε'_r value. The measurement was carried out using an open-ended coaxial probe and a network analyzer in the range of 0.5−4.5 GHz to study properties including the relative dielectric constant $(\varepsilon'_r$, the real part of complex permittivity) and the relative dielectric loss factor $(\varepsilon''_r$, the imaginary part of complex permittivity). The data collection was performed inside a custom-built chamber designed to maintain a circumferentially uniform illumination environment during the measurement by a reflecting half-circular aluminum plate installed at the back surface of the chamber. Illumination periods were chosen to be 60 min in consistent with that used in our previous reports.[1,2]

Because our objective of these measurements was to investigate the dielectric amplification of core−shell nanoparticle constructs in response to internally photoinduced generation of SPR energy within the intermediate Au shell layer, we selected a white LED light with the output power of 2.0 W for the study. Its emission photoenergy output spectrum matched mainly with optical absorptions of DPAF-C$_9$ and the Au layer. The steady-state absorption peak maxima (λ_{max}) of the C$_{60}$> cage and TMTTF derivative moieties are centered at 332 and 315 nm, respectively, outside the photoexcitation energy range of the light-emitting beams. These two components may not be involved directly in initial photo-excitation events. Therefore, the collected data should be correlated with the photoinduced e$^-$ transfer mechanism, as discussed above, to begin mostly from internal generation of the SPR energy, followed by the interlayer transfer of such energy to the outer layers to induce the subsequent intramolecular and intermolecular e$^-$-transfer events, leading to the electron polarization of the nanoparticle system.

As a result, Figure 6A showed irradiation time-dependent relative dielectric constant (ε'_r) curves of (**11-NPs**) @$(\text{TMTTF})_m$ (**12-NPs**) having various molar ratios of TMTTF to the C$_{60}$> moiety in the structure of the nanoparticle, taken at the microwave frequency of 1.0 GHz
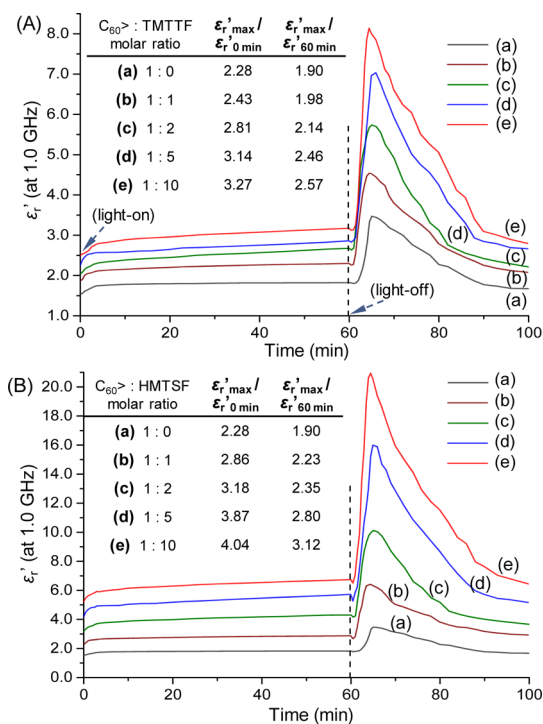

Figure 6. Irradiation time-dependent relative dielectric constant (ε'_r) amplification of tetralayered core−shell nanoparticles of (A) $(\gamma\text{-FeO}_x@\text{AuNP})@[\text{C}_{60}(>\text{DPAF-C}_9)]_n@(\text{TMTTF})_m$ (**12-NPs**) and (B) (**11-NPs**)@$(\text{HMTSF})_m$ (**18-NPs**) with various molar ratios of TMTTF or HMTSF molecules, respectively, to the C$_{60}$> moiety at the frequency of 1.0 GHz. White LED light irradiation period was 60 min.

during and after a 60 min illumination (corresponding to a total light fluence of 12.8 J/cm^2). It is interesting to note that the detected initial dielectric constant value of a sample mixture at the time zero min was comparable in value to that of C$_{60}$(>DPAF-C$_9$) and TMTTF as composites even though the inner shell layer of AuNPs and the core γ-FeO$_x$ NPs consisted of a significant quantity of material counts. A much higher ε'_r (=9.0) value of AuNPs was not visible, only very outer layers of soft materials dominated the measured dielectric property. In all experiments, white light illumination led to a slight rise in temperature to 35−45 °C in the first 6.0 min. A slight increase of chamber temperatures away from 25 °C resulted in a small increase of the ε'_r value in a similar degree among all samples. The ε'_r value was then remaining relatively steady during the rest of the irradiation period up to 60 min. Apparently, an incremental increase of the TMTTF quantity deposited at the outer shell layer of the nanoparticle gave a small progressive increase of the initial ε'_{r0} value at the time zero min of irradiation. Upon turning-off the light at the end of 60 min irradiation, we observed a large sharp raise of the ε'_r value for all samples in Figure 6A, whereas the chamber temperature dropped quickly back to 25 °C. Sharp increase of the permittivity at the light-off stage was found to reach a peak maximum $(\varepsilon'_{r\,max})$ value of 3.47 for **11-NPs** (Figure 6Aa) and 4.53 (Figure 6Ab), 5.73 (Figure 6Ac), 7.03 (Figure 6Ad), and 8.14 (Figure 6Ae) for four **12-NPs** samples having a C$_{60}$>/TMTTF molar ratio of 1:1, 1:2, 1:5, and 1:10, respectively. They can be accounted by a ratio of $\varepsilon'_{r\,max}/\varepsilon'_{r\,0min}$ ($\varepsilon'_{r\,0min}$ = 1.52 at 1.0 GHz and time zero) in a 2.28-fold increase for **11-NPs**. This $\varepsilon'_{r\,max}/\varepsilon'_{r\,0min}$ ratio of Figure 6Ab ($\varepsilon'_{r\,0min}$ = 1.86), 6Ac

($\varepsilon'_{r\,0min}$ = 2.04), 6Ad ($\varepsilon'_{r\,0min}$ = 2.24), and 6Ae ($\varepsilon'_{r\,0min}$ = 2.49) was calculated to be in a 2.43-, 2.81-, 3.14-, and 3.27-fold increase, respectively. Similar calculations based on the ratio of $\varepsilon'_{r\,max}/\varepsilon'_{r\,60min}$ (the ε'_r value at time 60 min) were found to be 1.90-, 1.98-, 2.14-, 2.46-, and 2.57-fold increase in the ε'_r value for 11-NPs ($\varepsilon'_{r\,60min}$ = 1.82), Figure 6Ab ($\varepsilon'_{r\,60min}$ = 2.29), 6Ac ($\varepsilon'_{r\,60min}$ = 2.68), 6Ad ($\varepsilon'_{r\,60min}$ = 2.85), and 6Ae ($\varepsilon'_{r\,60min}$ = 3.16), respectively.

In the case of (11-NPs)@(HMTSF)$_m$ (18-NPs) based on the same C$_{60}$>/HMTSF molar ratio of 1:1, 1:2, 1:5, and 1:10, an even larger increase of permittivity at the light-off stage was detected to reach a peak maximum ($\varepsilon'_{r\,amx}$) value of 6.38 (Figure 6Bb, $\varepsilon'_{r\,0min}$ = 2.23), 10.11 (Figure 6Bc, $\varepsilon'_{r\,0min}$ = 3.18), 15.98 (Figure 6Bd, $\varepsilon'_{r\,0min}$ = 4.14), and 20.94 (Figure 6Be, $\varepsilon'_{r\,0min}$ = 5.18), respectively. These values corresponded to a $\varepsilon'_{rmax}/\varepsilon'_{r\,0min}$ ratio of 2.86-, 3.18-, 3.87-, and 4.04-fold increase. The initial $\varepsilon'_{r\,0min}$ values of 18-NP-based samples were higher than those of 12-NPs as compared with the same molar quantity of e$^-$ donors applied owing to higher polarizability of selenium than sulfur. The data indicated gradually less contributions to the dielectric amplification with a larger quantity of HMTSF applied. For example, the calculated $\varepsilon'_{r\,max}$ increase per an additional 1.0 equiv of HMTSF to C$_{60}$> added was found to be 58, 32, 23, and 3.4% in value at the C$_{60}$>/HMTSF molar ratio of 1:1, 1:2, 1:5, and 1:10, respectively, with a sharp drop at a molar ratio from 5.0 to 10 equiv of HMTSF applied. This was indicative of a saturation effect of C$_{60}$> cages to accept no more than 3.0 equiv of electrons per cage, agree well with the detected three reversible redox potential cycles of C$_{60}$> (Figure 5b).

These results obviously provided an evidence showing a clear progressively enhanced photoswitch-on dielectric property or permittivity amplification phenomena upon the gradual increase of the e$^-$ donor in quantity. The observation agreed well with the fact that more TMTTF or HMTSF molecules applied in a larger quantity before saturation should provide more electron sources for donation to result in a larger number of polarized negative charges [(C$_{60}$>)$^{-\bullet}$] within the C$_{60}$(>DPAF-C$_9$)-derived fullerosome membrane of a multi-layered core−shell nanospherical particle and positive charges [(TMTTF)$^{+\bullet}$] or [(HMTSF)$^{+\bullet}$] outside the fullerosome. These charge pairs in an increased quantity located at separated shell layers may become the foundation of detected dielectric property enhancement to support our hypothesis of inter-molecular e$^-$-transfer mechanism stated above.

We also investigated the donor-dependent dielectric property of tetralayered (11-NPs)@(e$^-$-donor)$_m$ nanoparticles by selecting five organic molecular e$^-$-donor chromophores, such as TMTTF (3), TMSeTTF (4), TPSeTTF (5), BEDT-TTF (6), and HMTSF (7), and three forms of conducting polymers, such as P3HT (8), emeraldine PANi (9), and doped PANi-CSA (10) for comparison. Each compound has its own characteristic oxidation potentials that govern the relative strength in releasing one or two electrons to C$_{60}$>. Compounds TTF, TMTTF, and its derivatives[53,54] were recognized as strong π-electron donors to yield highly conductive materials. Its planar nonaromatic 7-π-electron system per a half fulvalene ring can be oxidized easily by removing one electron to afford an aromatic 6-π-electron system reversibly, giving the cation radical (TMTTF)$^{+\bullet}$ at relatively low redox potentials ($^1E_{1/2}$ = 0.45 V vs Ag/Ag$^+$, Figure 5a). Subsequent removal of the second electron from the second half of the fulvalene ring gave a fully aromatic dicationic (TMTTF)$^{2+}$ with a total of 12-π-

electrons. Therefore, these cationic and dicationic forms are thermodynamically stable species with large stabilization arising from the versatility and tendency of lone pairs of sulfur atoms to be eliminated. This tendency facilitated their electron-donating ability. Attachment of e$^-$-donating or e$^-$-withdrawing alkyl or phenyl groups to TTF leading to TMSeTTF, TPSeTTF, and BEDT-TTF can modify their potentials in oxidation−reduction cycles of voltammograms. In addition, chemical conversion of TTF to its tetraselenafulvalene analogues, such as HMTSF, may give great advantages with respect to the enhanced polarizability, conduction bandwidth, and intermolecular interactions with an increasing van der Waals radius from those of the tetrathia-analogues.[55−57]

To demonstrate the donor-dependent effect, we fixed the molar ratio of C$_{60}$> versus e$^-$ donor at 1:5 in the comparison. As a result, deposition of these five molecular e$^-$ donors (3, 4, 5, 6, and 7) individually onto trilayered 11-NPs giving the corresponding tetralayered core−shell (11-NPs)@(e$^-$-donor)$_m$ as 12-NPs, 15-NPs, 16-NPs, 17-NPs, and 18-NPs, respectively, exhibited similar photoswitchable dielectric property amplification phenomena (Figure 7A) at the permittivity maximum in
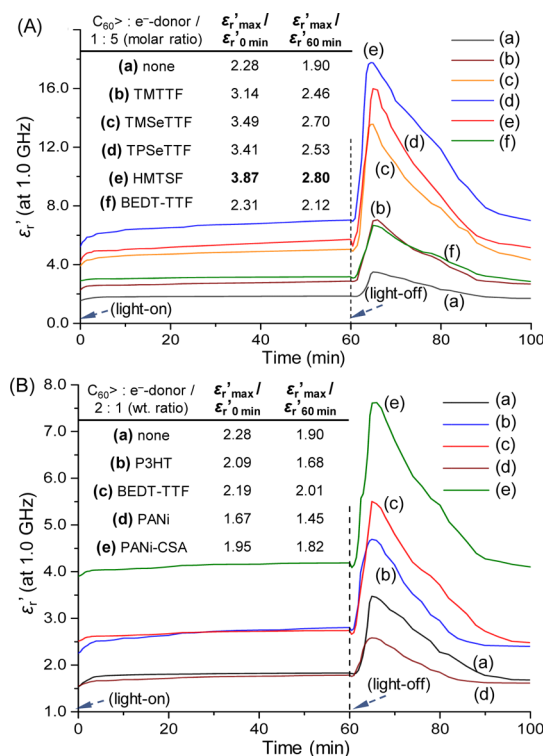

C$_{60}$> : e$^-$-donor / 1 : 5 (molar ratio)	$\varepsilon'_{r\,max}/\varepsilon'_{r\,0\,min}$	$\varepsilon'_{r\,max}/\varepsilon'_{r\,60\,min}$
(a) none	2.28	1.90
(b) TMTTF	3.14	2.46
(c) TMSeTTF	3.49	2.70
(d) TPSeTTF	3.41	2.53
(e) HMTSF	**3.87**	**2.80**
(f) BEDT-TTF	2.31	2.12

C$_{60}$> : e$^-$-donor / 2 : 1 (wt. ratio)	$\varepsilon'_{r\,max}/\varepsilon'_{r\,0\,min}$	$\varepsilon'_{r\,max}/\varepsilon'_{r\,60\,min}$
(a) none	2.28	1.90
(b) P3HT	2.09	1.68
(c) BEDT-TTF	2.19	2.01
(d) PANi	1.67	1.45
(e) PANi-CSA	1.95	1.82

Figure 7. Large sharp irradiation time-dependent amplification of relative dielectric constant (ε'_r, or permittivity) of tetralayered core−shell (A) (a) 11-NPs, (b) 12-NPs, (c) 15-NPs, (d) 16-NPs, (e) 18-NPs, and (f) 17-NPs with a molar ratio of the C$_{60}$> moiety to e$^-$ donor as 1:5. (B) (a) 11-NPs, (b) 19-NPs, (c) 17-NPs, (d) 20-NPs, and (e) 21-NPs with a weight ratio of the C$_{60}$> moiety to e$^-$-donor polymer as 2:1. The microwave frequency of 1.0 GHz was applied with a white LED light irradiation period of 60 min.

less than 7.0 min after the light being turned off. It was followed by a relaxation process of ε'_r back to a value of 1.5−3.5 nearly identical to the initial $\varepsilon'_{r\,0min}$ value, indicating effective recyclability of photoswitchable characteristics during light-on and light-off cycles. The $\varepsilon'_{r\,0min}$ value of organic e$^-$ donors was higher than that of C$_{60}$(>DPAF-C$_9$) as 1.52. By taking the

dielectric constant $\varepsilon'_{r\,0min}$ of TMTTF, TMSeTTF, TPSeTTF, BEDT-TTF, and HMTSF at the time zero as the reference, the maximum permittivity ($\varepsilon'_{r\,max}$) magnitude of 7.03 (Figure 7Ab, $\varepsilon'_{r\,0min}$ = 2.23), 13.55 (Figure 7Ac, $\varepsilon'_{r\,0min}$ = 3.88), 17.75 (Figure 7Ad, $\varepsilon'_{r\,0min}$ = 5.20), 6.66 (Figure 7Af, $\varepsilon'_{r\,0min}$ = 2.88), and 15.98 (Figure 7Ae, $\varepsilon'_{r\,0min}$ = 4.14), respectively, at the time 67 min indicated a 86, 121, 113, 3, and 159%, respectively, further increase of the $\varepsilon'_{r\,amx}/\varepsilon'_{r\,0min}$ ratio from that of **11**-NPS (2.28, Figure 7Aa). The data showed the highest dielectric amplification by using HMTSF molecules as the electron supplements, followed by the order of TMSeTTF ≈ TPSeTTF > TMTTF > BEDT-TTF. The relatively low contribution of BEDT-TTF was rather unexpected because it was reported to exhibit superconductivity in a form of κ-(BEDT-TTF)$_2$Cu[N-(CN)$_2$]Br complex salt.[16,58] Three forms of conducting polymers were also investigated in a weight ratio of 2:1 for C$_{60}$>/e$^-$-donor polymer (a unit weight of C$_{60}$> as 720 is much higher than that of each monomer unit of the polymer) for comparison with the dielectric contribution of BEDT-TTF, as shown in Figure 7B. We found that they were either in the similar range of dielectric amplification or even lower in efficiency than BEDT-TTF. A comparable amplification performance of (**11**-NPs)@(P3HT)$_m$ (**19**-NPs, Figure 7Bb) to that of (**11**-NPs)@(BEDT-TTF)$_m$ (**17**-NPs) was rather contradictory to our prediction because P3HT (**8**) was extensively studied in the fabrication of highly efficient organic photovoltaic cells in conjunction with e$^-$-acceptor PCBM (a monoadduct of C$_{60}$) to provide a significant quantity of photocurrent under solar exposure.[59−61] Perhaps, other factors than redox potentials of P3HT were involved. Considering a long chain length of P3HT, only a small portion of the repeating thiophene units can be positioned in direct physical contact with the fullerosome layer of the nanoparticle. This limited the number of charges to be generated at the interface area. Similar conclusions were made for the use of polyaniline in an emeraldine base form (PANi, **9**). When neutral PANi was doped by camphor sulfonic acid to its conducting form (PANi-CSA, **10**), a larger value of $\varepsilon'_{r\,0min}$ as 3.90 at the time zero was detected owing to a higher electronic conductivity. However, the dielectric amplification efficiency of (**11**-NPs)@(PANi-CSA)$_m$ (**21**-NPs) was also found in the range similar to that of **17**-NPs.

CONCLUSIONS

We demonstrated that the fabrication of tetralayered e$^-$-polarizable core−shell nanostructures was capable of inducing photoswitchable dielectric property (permittivity) amplification at the microwave frequency range of 1.0−4.0 GHz. Configuration of the nanostructure consisted of a magnetic nanospherical center core of γ-FeO$_x$ NP encapsulated sequentially by one plasmonic gold subshell, one middle layer of e$^-$-polarizable C$_{60}$(>DPAF-C$_n$)$_x$-derived fullerosome membrane, and one outer shell of e$^-$ donors, as an example. This class of multilayered core−shell nanospherical materials was reported recently to be excellent microwave absorbers over 1.0−18 GHz with the reflectivity loss reaching −28 to −36 dB at 6.0, 8.0, 12.0, 15.2, and 15.5 GHz, using S_{11} scattering parameter measurements and over −60 to −75 dB at higher frequencies of 17−18 GHz using angle-dependent S_{21} scattering parameter measurements.[1] Contribution of SPR energy within the core−shell nanoparticle structure[62−64] was the critical factor to the observed results. We hypothesized that the release of accumulated SPR energy at the near field from

the intermediate AuNP layer sandwiched between the layer of fullerosome membrane and the core γ-FeO$_x$ NP induced the molecular polarization of C$_{60}$(>DPAF-C$_9$)$_x$ moieties to their transient CS states. This CS state consisting of a positively charged e$^-$-donor moiety (DPAF)$^{+•}$-C$_9$ and a negatively charged e$^-$-acceptor moiety (C$_{60}$>)$^{−•}$ provided the foundation of observed dielectric property amplification. The phenomena were further enhanced by separate applications of additional organic molecular e$^-$ donors or conducting conjugate polymers deposited at the most outer shell layer. These e$^-$ donors served as the supply of photoinduced transferrable electrons that increased largely the number of polarized charges on nanoparticles, leading to a maximum of 387% amplification of the relative dielectric constant (ε'_r) value or a 159% additional increase from that of the parent trilayered **11**-NPs. These results were contributed from the use of organic e$^-$-donor HMTSF molecules.

On the basis of our previous investigation and results of facile photoswitchable tunability of reflective microwave signals using monostatic and angle-dependent bistatic synthetic aperture techniques based on **11**-NP-casted thin films in the frequency range of 0.5−18 GHz,[1,2] we expect better performance given by the new tetralayered core−shell NPs. It is based on the fact that the largely enhanced permittivity from that of **11**-NPs was obtained by the current e$^-$-donor approach. As the Wi-Fi wireless network communication being operated at either 2.4 or new 5.0 GHz frequency band, they are within the frequency range of this investigation. Therefore, our results may lead to future implication on the feasibility in modulation or tuning microwave signals by **18**-NPs to provide photoswitchable interference for the security protection purpose.

■ ASSOCIATED CONTENT

Ⓢ Supporting Information

The Supporting Information is available free of charge on the ACS Publications website at DOI: 10.1021/acs.jpcc.8b02676.

Synthetic procedures of e$^-$-donors C$_{60}$(>DPAF-C$_9$), 2,3,6,7-tetrakis(methylseleno)-tetrathiafulvalene (TMSeTTF), 2,3,6,7-tetrakis(phenylseleno)-tetrathiafulvalene (TPSeTTF), and HMTSF; ^{1}H NMR spectra of 2,3,6,7-tetramethyltetrathiafulvalene (TMTTF), TMSeTTF, and TPSeTTF; cyclic voltammograms of HMTSF, BEDT-TTF, TPSeTTF, TMSeTTF, and TMTTF; infrared (FT-IR) spectra of trilayered (γ-FeO$_x$@AuNP)@[C$_{60}$(>DPAF-C$_9$)$_x$]$_n$ (**11**-NPs), TMTTF, tetralayered (γ-FeO$_x$@AuNP)@[C$_{60}$(>DPAF-C$_9$)]$_n$@(TMTTF)$_m$ (**12**-NPs), TMSeTTF, tetralayered (**11**-NPs)@(TMSeTTF)$_m$ (**15**-NPs), TPSeTTF, tetralayered (**11**-NPs)@(TPSeTTF)$_m$ (**16**-NPs), HMTSF (**7**), and tetralayered (**11**-NPs)@(HMTSF)$_m$ (**18**-NPs); and dielectric (permittivity) measurement diagram (PDF)

■ AUTHOR INFORMATION

Corresponding Author

*E-mail: Long_Chiang@uml.edu. Phone: 978-934-3663. Fax: 978-934-3013 (L.Y.C.).

ORCID Ⓘ

Loon-Seng Tan: 0000-0002-2134-9290
Long Y. Chiang: 0000-0003-0097-5118

Author Contributions

All authors contributed equally to this work.

■ REFERENCES

(1) Wang, M.; Yu, T.; Tan, L.-S.; Urbas, A.; Chiang, L. Y. Tunability of RF-Responses by Plasmonic Dielectric Amplification Using Branched e−-Polarizable C_{60}-adducts on Magnetic Nanoparticles. *J. Phys. Chem. C* **2016**, *120*, 17711−17721.

(2) Wang, M.; Su, C.; Yu, T.; Tan, L.-S.; Hu, B.; Urbas, A.; Chiang, L. Y. Novel Photoswitchable Dielectric Properties on Nanomaterials of Electronic Core-Shell γ-FeOx@Au@fullerosomes for GHz Frequency Applications. *Nanoscale* **2016**, *8*, 6589−6599.

(3) Chiang, L. Y.; Padmawar, P. A.; Rogers-Haley, J. E.; So, G.; Canteenwala, T.; Thota, S.; Tan, L.-S.; Pritzker, K.; Huang, Y.-Y.; Sharma, S. K.; et al. Synthesis and Characterization of Highly Photoresponsive Fullerenyl Dyads with a Close Chromophore Antenna−C_{60} Contact and Effective Photodynamic Potential. *J. Mater. Chem.* **2010**, *20*, 5280−5293.

(4) El-Khouly, M. E.; Anandakathir, R.; Ito, O.; Chiang, L. Y. Prolonged Photoinduced Charge-Separated States in Starburst Tetra-(diphenylaminofluoreno)[60]fullerene Adducts. *J. Phys. Chem. A* **2007**, *111*, 6938−6944.

(5) Novotny, L.; Hecht, B. *Principle of Nano-Optics*; Cambridge University Press: New York, 2006, references therein.

(6) Mertz, J. Radiative Absorption, Fluorescence, and Scattering of a Classical Dipole Near a Lossless Interface: an Unified Description. *J. Opt. Soc. Am. B* **2000**, *17*, 1906−1913.

(7) Luk'yanchuk, B.; Zheludev, N. I.; Maier, S. A.; Halas, N. J.; Nordlander, P.; Giessen, H.; Chong, C. T. The Fano Resonance in Plasmonic Nanostructures and Metmaterials. *Nat. Mater.* **2010**, *9*, 707−715.

(8) Wang, M.; Jeon, S.; Su, C.; Yu, T.; Tan, L.-S.; Chiang, L. Synthesis of Photoswitchable Magnetic Au−Fullerosome Hybrid Nanomaterials for Permittivity Enhancement Applications. *Molecules* **2015**, *20*, 14746−14760.

(9) Wudl, F.; Wobschall, D.; Hufnagel, E. J. Electrical Conductivity by the Bis(1,3-dithiole)-bis(1,3-dithiolium) System. *J. Am. Chem. Soc.* **1972**, *94*, 670−672.

(10) Ferraris, J.; Cowan, D. O.; Walatka, V.; Perlstein, J. H. Electron Transfer in a New Highly Conducting Donor−Acceptor Complex. *J. Am. Chem. Soc.* **1973**, *95*, 948−949.

(11) Jérome, D. Organic Conductors: From Charge Density Wave TTF−TCNQ to Superconducting $(TMTSF)_2PF_6$. *Chem. Rev.* **2004**, *104*, 5565−5592.

(12) Torrance, J. B.; Mayerle, J. J.; Lee, V. Y.; Bozio, R.; Pecile, C. Anomalous Properties of New Organic Conductors: Comparison of Bromanil, Chloranil, and Tetracyanoquinodimethane (TCNQ) Salts of Tetramethyltetrathiafulvalene (TMTTF). *Solid State Commun.* **1981**, *38*, 1165−1169.

(13) Shu, P.; Chiang, L.; Emge, T.; Holt, D.; Kistenmacher, T.; Lee, M.; Stokes, J.; Poehler, T.; Bloch, A.; Cowan, D. Synthesis of 2,2′-Bithieno[3,4-d]-1,3-dithiole (DTTTF) and Some of Its Charge Transfer Salts. *J. Chem. Soc., Chem. Commun.* **1981**, 920.

(14) Chiang, L. Y.; Shu, P.; Holt, D.; Cowan, D. O. Chemistry en-Route to 2,2′-Bithieno[3,4-d]-1,3-dithiol (DTTTF) and Its Selenium Analogue. *J. Org. Chem.* **1983**, *48*, 4713−4717.

(15) Seo, H.; Hotta, C.; Fukuyama, H. Toward Systematic Understanding of Diversity of Electronic Properties in Low-Dimensional Molecular Solids. *Chem. Rev.* **2004**, *104*, 5005−5036.

(16) Kini, A. M.; Geiser, U.; Wang, H. H.; Carlson, K. D.; Williams, J. M.; Kwok, W. K.; Vandervoort, K. G.; Thompson, J. E.; Stupka, D. L. A New Ambient-Pressure Organic Superconductor, κ-$(ET)_2Cu[N-(CN)_2]Br$, with the Highest Transition Temperature Yet Observed (Inductive Onset T, = 11.6 K, Resistive Onset = 12.5 K). *Inorg. Chem.* **1990**, *29*, 2555−2557.

(17) Gubser, D. U.; Fuller, W. W.; Poehler, T. O.; Cowan, D. O.; Lee, M.; Potember, R. S.; Chiang, L.-Y.; Bloch, A. N. Magnetic Susceptibility and Resistive Transitions of Superconducting (TMTSF)2ClO4: Critical Magnetic Fields. *Phys. Rev. B: Condens. Matter Mater. Phys.* **1981**, *24*, 478−480.

(18) Naughton, M. J.; Brooks, J. S.; Chiang, L. Y.; Chamberlin, R. V.; Chaikin, P. M. Magnetization Study of the Field-Induced Transitions in Tetramethyltetraselenafulvalenium Perchlorate, (TMTSF)2ClO4. *Phys. Rev. Lett.* **1985**, *55*, 969−972.

(19) Wosnitza, J. Superconductivity in Layered Organic Metals. *Crystals* **2012**, *2*, 248−265.

(20) Bailey, A. B.; McCullough, R. D.; Mays, M. D.; Cowan, D. O.; Lerstrup, K. A. New Organic π-Donors: Analogues of HMTSF and HMTTeF. *Synth. Met.* **1988**, *27*, 425−430.

(21) Saito, G.; Yoshida, Y. Development of Conductive Organic Molecular Assemblies: Organic Metals, Superconductors, and Exotic Functional Materials. *Bull. Chem. Soc. Jpn.* **2007**, *80*, 1−137.

(22) Kreher, D.; Hudhomme, P.; Gorgues, A.; Luo, H.; Araki, Y.; Ito, O. Photoinduced Electron Transfer Processes of a Fused C_{60}−TTF−C_{60} Dumbbell Triad. *Phys. Chem. Chem. Phys.* **2003**, *5*, 4583−4592.

(23) Martín, N.; Sánchez, L.; Herranz, M. A.; Illescas, B.; Guldi, D. M. Electronic Communication in Tetrathiafulvalene (TTF)/C_{60} Systems: Toward Molecular Solar Energy Conversion Materials? *Acc. Chem. Res.* **2007**, *40*, 1015−1024.

(24) Guldi, D. M.; Prato, M. Excited-State Properties of C_{60} Fullerene Derivatives. *Acc. Chem. Res.* **2000**, *33*, 695−703.

(25) Martín, N.; Sánchez, L.; Herranz, M. A.; Guldi, D. M. Evidence for Two Separate One-Electron Transfer Events in Excited Fulleropyrrolidine Dyads Containing Tetrathiafulvalene (TTF). *J. Phys. Chem. A* **2000**, *104*, 4648−4657.

(26) Ito, O. Photosensitizing Electron Transfer Processes of Fullerenes, Carbon Nanotubes, and Carbon Nanohorns. *Chem. Rec.* **2017**, *17*, 326−362.

(27) Thomas, K. G.; George, M. V.; Kamat, P. V. Photoinduced Electron Transfer Processes in Fullerene-Based Donor-Acceptor Systems. *Helv. Chim. Acta* **2005**, *88*, 1291−1308.

(28) Fukuzumi, S.; Ohkubo, K.; Imahori, H.; Guldi, D. M. Driving Force Dependence of Intermolecular Electron-Transfer Reactions of Fullerenes. *Chem.—Eur. J.* **2003**, *9*, 1585−1593.

(29) Kreher, D.; Hudhomme, P.; Gorgues, A.; Luo, H.; Araki, Y.; Ito, O. *Phys. Chem. Chem. Phys.* **2003**, *5*, 4583−4592.

(30) Kirner, S.; Sekita, M.; Guldi, D. M. 25th Anniversary Article: 25 Years of Fullerene Research in Electron Transfer Chemistry. *Adv. Mater.* **2014**, *26*, 1482−1493.

(31) Sariciftci, N. S.; Smilowitz, L.; Heeger, A. J.; Wudl, F. Photoinduced Electron Transfer from a Conducting Polymer to Buckminsterfullerene. *Science* **1992**, *258*, 1474−1476.

(32) Kanibolotsky, A. L.; Findlay, N. J.; Skabara, P. J. Polythiophene and Oligothiophene Systems Modified by TTF Electroactive Units for Organic Electronics. *Beilstein J. Org. Chem.* **2015**, *11*, 1749−1766.

(33) Luo, H.; Fujitsuka, M.; Araki, Y.; Ito, O.; Padmawar, P.; Chiang, L. Y. Inter- and Intramolecular Photoinduced Electron-Transfer Processes Between C_{60} and Diphenylaminofluorene in Solutions. *J. Phys. Chem. B* **2003**, *107*, 9312−9318.

(34) Padmawar, P. A.; Rogers, J. E.; He, G. S.; Chiang, L. Y.; Tan, L.-S.; Canteenwala, T.; Zheng, Q.; Slagle, J. E.; et al. Large Cross-Section Enhancement and Intramolecular Energy Transfer upon Multiphoton Absorption of Hindered Diphenylaminofluorene-C_{60} Dyads and Triads. *Chem. Mater.* **2006**, *18*, 4065−4074.

(35) Chiang, L.-Y.; Poehler, T. O.; Bloch, A. N.; Cowan, D. O. The Modified Synthesis of Tetraselenafulvalenes. *J. Chem. Soc., Chem. Commun.* **1980**, 866b.

(36) Hsu, S. Y.; Chiang, L. Y. An Efficient Synthesis of Alkyl and Aryl Chalcogenated Derivatives of Tetrathiafulvalene. *J. Org. Chem.* **1987**, *52*, 3444−3446.

(37) Cowan, D. O.; Kini, A.; Chiang, L.-Y.; Lerstrup, K. The Design, Synthesis and Characterization of the Molecular Components of Organic Conductors. *Mol. Cryst. Liq. Cryst.* **1982**, *86*, 1−26.

(38) Okada, N.; Yamochi, H.; Shinozaki, F. Tetrakis(n-alkyltelluro)-tetrathiafulvalene (TTeC$_n$-TTF). *Chem. Lett.* **1986**, *15*, 1861−1864.

(39) Yamochi, H.; Iwasawa, N.; Urayama, H.; Saito, G. Synthesis and Properties of Tetrakis(alkylseleno)tetrathiafulvalene. *Chem. Lett.* **1987**, *16*, 2265−2268.

(40) Okamoto, Y.; Lee, H. S.; Attarwala, S. T. Synthesis and Reactivities of Trimethylsilyl-Substituted Tetrathia- and Tetraselena-fulvalenes. *J. Org. Chem.* **1985**, *50*, 2788−2790.

(41) Jiang, B.; Pang, X.; Li, B.; Lin, Z. Organic−Inorganic Nanocomposites via Placing Monodisperse Ferroelectric Nanocrystals in Direct and Permanent Contact with Ferroelectric Polymers. *J. Am. Chem. Soc.* **2015**, *137*, 11760−11767.

(42) Pang, X.; He, Y.; Jung, J.; Lin, Z. 1D Nanocrystals with Precisely Controlled Dimensions, Compositions, and Architectures. *Science* **2016**, *353*, 1268−1272.

(43) Chen, Y.; Yang, D.; Yoon, Y. J.; Pang, X.; Wang, Z.; Jung, J.; He, Y.; Harn, Y. W.; He, M.; Zhang, S.; et al. Hairy Uniform Permanently Ligated Hollow Nanoparticles with Precise Dimension Control and Tunable Optical Properties. *J. Am. Chem. Soc.* **2017**, *139*, 12956−12967.

(44) He, Y.; Pang, X.; Jiang, B.; Feng, C.; Harn, Y.-W.; Chen, Y.; Yoon, J. Y.; Pan, S.; Lu, C.-H.; Chang, Y.; et al. Unconventional Route to Uniform Hollow Semiconducting Nanoparticles with Tailorable Dimensions, Compositions, Surface Chemistry, and Near-Infrared Absorption. *Angew. Chem., Int. Ed.* **2017**, *56*, 12946−12951.

(45) Li, X.; Iocozzia, J.; Chen, Y.; Zhao, S.; Cui, X.; Wang, W.; Yu, H.; Lin, S.; Lin, Z. From Precision Synthesis of Block Copolymers to Properties and Applications of Nanoparticles. *Angew. Chem., Int. Ed.* **2018**, *57*, 2046−2070.

(46) Verma, S.; Hauck, T.; El-Khouly, M. E.; Padmawar, P. A.; Canteenwala, T.; Pritzker, K.; Ito, O.; Chiang, L. Y. Self-Assembled Photoresponsive Amphiphilic Diphenylaminofluorene-C$_{60}$ Conjugate Vesicles in Aqueous Solution. *Langmuir* **2005**, *21*, 3267−3272.

(47) Ohno, T. R.; Chen, Y.; Harvey, S. E.; Kroll, G. H.; Weaver, J. H.; Haufler, R. E.; Smalley, R. E. C$_{60}$ Bonding and Energy-Level Alignment on Metal and Semiconductor Surfaces. *Phys. Rev. B: Condens. Matter Mater. Phys.* **1991**, *44*, 13747−13755.

(48) Yong, V.; Hahn, H. T. Synergistic Effect of Fullerene-Capped Gold Nanoparticles on Graphene Electrochemical Supercapacitors. *Adv. Nanopart.* **2013**, *02*, 1−5.

(49) Islam, M. T.; Molugu, S. K.; Cooke, P. H.; Noveron, J. C. Fullerene Stabilized Gold Nanoparticles. *New J. Chem.* **2015**, *39*, 5923.

(50) Kuzume, A.; Herrero, E.; Feliu, J. M.; Nichols, R. J.; Schiffrin, D. J. Fullerene Monolayers Adsorbed on High Index Gold Single Crystal Surfaces. *Phys. Chem. Chem. Phys.* **2004**, *6*, 619−625.

(51) Bubnis, G. J.; Cleary, S. M.; Mayne, H. R. Self-Assembly and Structural Behavior of a Model Rigid C$_{60}$-Terminated Thiolate on Au(111). *Chem. Phys. Lett.* **2009**, *470*, 289−294.

(52) Kang, N.-G.; Kokubo, K.; Jeon, S.; Wang, M.; Lee, C.-L.; Canteenwala, T.; Tan, L.-S.; Chiang, L. Synthesis and Photo-luminescent Properties of Geometrically Hindered cis-Tris-(diphenylaminofluorene) as Precursors to Light-Emitting Devices. *Molecules* **2015**, *20*, 4635−4654.

(53) Bendikov, M.; Wudl, F.; Perepichka, D. F. Tetrathiafulvalenes, Oligoacenenes, and Their Buckminsterfullerene Derivatives: The Brick and Mortar of Organic Electronics. *Chem. Rev.* **2004**, *104*, 4891−4945.

(54) Jeppesen, J. O.; Nielsen, M. B.; Becher, N. J. Tetrathiafulvalene Cyclophanes and Cage Molecules. *Chem. Rev.* **2004**, *104*, 5115−5132.

(55) Saito, G.; Enoki, T.; Inokuchi, H.; Kumagai, H.; Tanaka, J. Organic Conductors: Electrical Properties of HMTTeF (Hexamethy-lenetetratellurafulvalene) Complexes. *Chem. Lett.* **1983**, *12*, 503−506.

(56) Pac, S.-S.; Saito, G. Peculiarity of Hexamethylenetetratellur-afulvalene (HMTTeF) Charge Transfer Complexes of Donor−Acceptor (D−A). *J. Solid State Chem.* **2002**, *168*, 486−496.

(57) McCullough, R. D.; Kok, G. B.; Lerstrup, K. A.; Cowan, D. O. Tetratellurafulvalene (TTeF). *J. Am. Chem. Soc.* **1987**, *109*, 4115−4116.

(58) Talham, D. R.; Kurmoo, M.; Day, P.; Obertelli, D. S.; Parker, I. D.; Friend, R. H. Magnetic Properties of the Organic Superconductor β-(BEDT-TTF)$_2$AuI$_2$. *J. Phys. C: Solid State Phys.* **1986**, *19*, L383.

(59) Yan, Y.; Liu, X.; Wang, T. Conjugated-Polymer Blends for Organic Photovoltaics: Rational Control of Vertical Stratification for High Performance. *Adv. Mater.* **2017**, *29*, 1601674.

(60) Mazzio, K. A.; Luscombe, C. K. The Future of Organic Photovoltaics. *Chem. Soc. Rev.* **2015**, *44*, 78−90.

(61) Hedley, G. J.; Ruseckas, A.; Samuel, I. D. W. Light Harvesting for Organic Photovoltaics. *Chem. Rev.* **2017**, *117*, 796−837.

(62) Zheng, D.; Pang, X.; Wang, M.; He, Y.; Lin, C.; Lin, Z. Unconventional Route to Hairy Plasmonic/Semiconductor Core/Shell Nanoparticles with Precisely Controlled Dimensions and Their Use in Solar Energy Conversion. *Chem. Mater.* **2015**, *27*, 5271−5278.

(63) Wang, M.; Pang, X.; Zheng, D.; He, Y.; Sun, L.; Lin, C.; Lin, Z. Nonepitaxial Growth of Uniform and Precisely Size-Tunable Core/Shell Nanoparticles and their Enhanced Plasmon-Driven Photo-catalysis. *J. Mater. Chem. A* **2016**, *4*, 7190−7199.

(64) Chen, Y.; Wang, Z.; He, Y.; Yoon, Y. J.; Jung, J.; Zhang, G.; Lin, Z. Light-Enabled Reversible Self-Assembly and Tunable Optical Properties of Stable Hairy Nanoparticles. *Proc. Natl. Acad. Sci. U.S.A.* **2018**, *115*, E1391−E1400.